



# A novel Z-scheme $\text{Ag}_3\text{VO}_4/\text{BiVO}_4$ heterojunction photocatalyst: Study on the excellent photocatalytic performance and photocatalytic mechanism

Wei Zhao<sup>a,b,c</sup>, Yue Feng<sup>a</sup>, Haibao Huang<sup>d</sup>, Pengcheng Zhou<sup>a</sup>, Jing Li<sup>a</sup>, Lili Zhang<sup>a</sup>, Benlin Dai<sup>a,\*</sup>, Jiming Xu<sup>a</sup>, Fengxia Zhu<sup>a,\*</sup>, Ni Sheng<sup>e</sup>, Dennis Y.C. Leung<sup>b,\*</sup>

<sup>a</sup> Jiangsu Key Laboratory for Biomass-based Energy and Enzyme Technology, Jiangsu Collaborative Innovation Center of Regional Modern Agriculture & Environmental Protection, School of Chemistry and Chemical Engineering, Huaiyin Normal University, Huaian, China

<sup>b</sup> Department of Mechanical Engineering, The University of Hong Kong, Pokfulam Road, Hong Kong

<sup>c</sup> School of Environment, Nanjing Normal University, Nanjing, PR China

<sup>d</sup> School of Environmental Science and Engineering, Sun Yat-Sen University, PR China

<sup>e</sup> School of Business, Macau University of Science and Technology, Avenida Wai Long, Taipa, PR, Macau

## ARTICLE INFO

### Keywords:

Bismuth vanadate

Z-scheme heterojunction photocatalyst

Photocatalytic reduction and oxidation

## ABSTRACT

A novel three-dimensional microspheres mediator-free Z-scheme  $\text{Ag}_3\text{VO}_4/\text{BiVO}_4$  heterojunction photocatalyst was successfully obtained for the first time. The photocatalytic performance of the as-prepared photocatalyst was systematically examined via the photocatalytic reduction of  $\text{Cr}^{6+}$  and oxidation of Bisphenol S under visible-light irradiation. Among these samples, 0.24- $\text{Ag}_3\text{VO}_4/\text{BiVO}_4$  exhibits the highest photocatalytic performances, the photocatalytic reduction and oxidation efficiency of 74.9 and 94.8%, respectively, can be achieved. The enhanced photocatalytic performance is attributed to the built-in electric field assisted charge transfer between the  $\text{Ag}_3\text{VO}_4$  and  $\text{BiVO}_4$ , and the increasing lifetime of the charge carrier confirmed by the results of time-resolved fluorescence spectra and photoelectrochemical measures. Moreover, based on the results of free radical scavenging activity test, and EPR experiments, it has been verified that the  $\text{Ag}_3\text{VO}_4/\text{BiVO}_4$  heterostructures follow a typical Z-scheme charge transfer mechanism rather than conventional type-II heterojunction charge transfer mechanism. Furthermore, the theoretical understanding of the underlying mechanism was also supported, while the energy band structure, and Fermi level were systematically calculated using the density functional theory approach. The results show that a built-in electric field directed from  $\text{Ag}_3\text{VO}_4$  to  $\text{BiVO}_4$  surface was established as an equalized Fermi level was reached, which benefits the separation of photogenerated charge carriers in the way of a Z-scheme charge transfer mechanism. The strategy to form the three-dimensional microspheres Z-scheme heterojunction photocatalyst may offer new insight into the Z-scheme charge transfer mechanism for applications in the field of solar energy conversion.

## 1. Introduction

Considering the factors that heavy metals and organic pollutants often exist in the effluent discharge, the removal of them can be a challenge and have important implications in environmental protections. Thanks for the photocatalytic technology which can utilize the characteristics of semiconductor oxide surface activation under illumination, to oxidate organic matter, and reduce heavy metal ions, which offers an opportunity to overcome the discharge problems [1–11]. Titanium dioxide is widely used for its biochemical inert, low cost, non-toxicity, chemical stability and other characteristics [12–17]. However, the application of  $\text{TiO}_2$  is seriously limited by some shortcomings such as the low utilization of solar energy. Therefore,

designing new and efficient photocatalyst that can utilize visible light is the focus in current photocatalysis studies [18–37].

Among the photocatalysts under investigation,  $\text{BiVO}_4$  that possesses good chemical stability, and nontoxicity has aroused widespread attention recently [38–41]. However, further enhancing its performance is restricted due to its small surface area and low ability to separate electron-hole pairs [42–48]. Researchers have made further efforts to overcome these shortcomings for practical application.

It has emerged as new and important research hotspots to tailor the performances of photocatalysts via changing the morphologies and structures of photocatalysts. To date there are considerable efforts to synthesize  $\text{BiVO}_4$  with different morphologies. For instance, He and his group [49] have synthesized the olive-like  $\text{BiVO}_4$  hierarchical

\* Corresponding authors.

E-mail addresses: [benlindai@hytc.edu.cn](mailto:benlindai@hytc.edu.cn) (B. Dai), [zhufengxia501@163.com](mailto:zhufengxia501@163.com) (F. Zhu), [ytleung@hku.hk](mailto:ytleung@hku.hk) (D.Y.C. Leung).

<https://doi.org/10.1016/j.apcatb.2019.01.001>

Received 17 October 2018; Received in revised form 14 December 2018; Accepted 1 January 2019

Available online 02 January 2019

0926-3373/ © 2019 Elsevier B.V. All rights reserved.

architecture via a hydrothermal method. Zhang et al. [50] have prepared BiVO<sub>4</sub> nanosheets with excellent photocatalytic activity. Among BiVO<sub>4</sub>, it is predicted that three-dimensional flower-like microsphere assembled by primary nanoplates can show superior photocatalytic performances because its large specific surface area can adsorb organic contaminants. Experimental results in this study also demonstrated that BiVO<sub>4</sub> microspheres have larger specific surface area compared with BiVO<sub>4</sub> particles.

Fabricating a photocatalyst with Z-scheme heterojunction structure can efficiently improve its catalytic activity. Recently, the Z-scheme photocatalyst has attracted much interest owing to its stronger redox capacity compared to the conventional type-II heterojunction photocatalyst. More positive VB and more negative CB potentials in the Z-scheme system can improve the transfer of photogenerated holes and electrons with strong oxidation and reduction ability to enhance the photoactivity [51–62]. Lately, several Z-scheme heterojunction photocatalysts have been designed, for example, Wang et al. have fabricated g-C<sub>3</sub>N<sub>4</sub>/BiVO<sub>4</sub> interface Z-scheme photocatalysts with strong redox ability [63]. Safaei et al. have prepared an efficient Z-scheme g-C<sub>3</sub>N<sub>4</sub>/BiVO<sub>4</sub> photocatalyst, which has boosted the performance of BiVO<sub>4</sub> by four times [64]. Zhou and co-workers suggested that the Z-scheme heterojunction CdS/BiVO<sub>4</sub> photocatalyst shows more than two times increase in photocatalytic H<sub>2</sub> generation rate compared to bare CdS [39]. These Z-scheme heterojunction photocatalysts all showed an enhanced separation of photogenerated charge carriers and redox ability. Therefore, the Z-scheme approach is more beneficial with reference to the heterojunction transfer mechanism for preserving the redox ability.

Based on the above discussion, the new and efficient BiVO<sub>4</sub> based photocatalyst with Z-scheme heterojunction structure can be obtained by making full use of the high specific surface area of flower-like microspheres and the efficient charge transfer of Z-scheme heterojunction. Importantly, Wang et al. [65] reported that Z-scheme BiVO<sub>4</sub>/porous graphite carbon nitride heterojunction achieved a higher separation efficiency of the photogenerated carriers. Thus, it looks very promising to improve the photocatalytic activity of BiVO<sub>4</sub> flower-like microspheres by loading co-catalysts to form a Z-scheme BiVO<sub>4</sub> based heterojunction structure. In this paper, we tested this hypothesis via facile fabricating a novel three-dimensional flower-like microspheres Z-scheme Ag<sub>3</sub>VO<sub>4</sub>/BiVO<sub>4</sub> heterojunction photocatalyst. The synthetic route for the sample is shown in Fig. S1. Such novel constructure has advantages such as the facile charge separation, and the high specific surface area. The photocatalytic performance of the as-prepared photocatalyst was systematically examined via the photocatalytic reduction of Cr<sup>6+</sup> and oxidation of Bisphenol S (BPS) under visible-light irradiation. Moreover, the Z-scheme photocatalysis mechanism of the novel Ag<sub>3</sub>VO<sub>4</sub>/BiVO<sub>4</sub> was verified by a series of characterization, including time-resolved fluorescence emission decay spectra, photocurrent measure, Mott-Schottky plot, Nyquist plot of electrochemical impedance spectroscopy, control experiments using scavengers, as well as stimulation methods, such as DFT and CASTEP code.

## 2. Experimental

### 2.1. Materials

Bi(NO<sub>3</sub>)<sub>3</sub>·5H<sub>2</sub>O, Na<sub>3</sub>VO<sub>4</sub>·12H<sub>2</sub>O, AgNO<sub>3</sub>, and other reagents were AR grade and obtained from Sinopharm Chemical Reagent Co., Ltd.

### 2.2. Synthesis

Preparation of BiVO<sub>4</sub> particles: Bi(NO<sub>3</sub>)<sub>3</sub>·5H<sub>2</sub>O and NH<sub>4</sub>VO<sub>3</sub> solutions (0.4 M) containing HNO<sub>3</sub> (1.84 M) were prepared separately. After mixing these two 100 mL solutions, 7.5 g of urea was added. The mixed solution was stirred at 100 °C for 8 h. Then the precipitation formed by the hydrolysis was washed by water, filtered, and dried at 80 °C.

Preparation of BiVO<sub>4</sub> microsphere: Bi(NO<sub>3</sub>)<sub>3</sub>·5H<sub>2</sub>O (60 mg) and Na<sub>3</sub>VO<sub>4</sub>·12H<sub>2</sub>O (100 mg) were mixed in water (40 mL) under the condition of ultrasound dispersion. Then the mixture was put into an autoclave and the hydrothermal condition was adopted at 160 °C for 8 h. The obtained product was washed with water and ethanol.

Preparation of the Z-scheme Ag<sub>3</sub>VO<sub>4</sub>/BiVO<sub>4</sub> heterojunction photocatalyst: 1 mmol BiVO<sub>4</sub> was dispersed in 50 mL ultrapure water under ultrasonic conditions. 0.72 mmol AgNO<sub>3</sub> was added in the above dispersed solution and the solution was stirred for 30 min. After that, 0.24 mmol Na<sub>3</sub>VO<sub>4</sub>·12H<sub>2</sub>O dissolved into 50 mL water was added dropwise to the above solution. The mixture was kept stirring for 3 h in the dark condition. The final composite was collected by centrifugation and washed as above. The as-synthesized mixture was referred as 0.24-Ag<sub>3</sub>VO<sub>4</sub>/BiVO<sub>4</sub>. The number of 0.24 represents the molar ratio of Ag<sub>3</sub>VO<sub>4</sub>:BiVO<sub>4</sub>. Similarly, 0.06-Ag<sub>3</sub>VO<sub>4</sub>/BiVO<sub>4</sub>, 0.12-Ag<sub>3</sub>VO<sub>4</sub>/BiVO<sub>4</sub> and 0.36-Ag<sub>3</sub>VO<sub>4</sub>/BiVO<sub>4</sub> were also synthesized by the above procedures.

### 2.3. Photocatalytic activities evaluation

BPS and Cr<sup>6+</sup> were taken as the degradation objectives for evaluating the photocatalytic performance of the catalyst under visible-light irradiation using a 500 W Xe lamp with a 420 nm cut-off filter. 0.02 g of the photocatalyst was dispersed in the 50 mL of BPS or Cr<sup>6+</sup> reaction solution (15 mg/L), and the pH value of the reaction solution were 5.28 and 5.15, respectively.

60 min dark stirred was maintained in order to achieve adsorption-desorption equilibrium. At given time intervals after initiation of visible light irradiation, 5 mL of samples were collected into centrifuge tubes, centrifuged and passed through 0.22-μm Millipore membrane. The filtrate was subsequently analyzed by a UV-vis spectrophotometer.

The apparent quantum efficiency (QE) was measured under the same photocatalytic reaction condition with irradiation light at 420 nm by using cut-off filter and 500 W Xe lamp, and the QE was calculated according to Eq. (1): QE [%] = (number of reacted electrons/numbers of incident photons) × 100 (1) The number of incident photons was measured by using a calibrated Si photodiode. As for the photocatalytic reduction of Cr<sup>6+</sup>, assuming that the reaction from Cr<sup>6+</sup> to Cr<sup>3+</sup> is proceeded: Cr<sub>2</sub>O<sub>7</sub><sup>2-</sup> + 14H<sup>+</sup> + 6e<sup>-</sup> → 2Cr<sup>3+</sup> + 7H<sub>2</sub>O E<sup>0</sup> = 0.98 eV/NHE (-5.48 eV/AVS), that is, 3 photons are required to produce one Cr<sup>3+</sup> molecule.

### 2.4. Material characterization

FT-IR spectra were recorded using a Perkin-Elmer FTIR Analyzer, and KBr was used to serve as a reference. XRD patterns of the samples were determined by an XRD-6000r, SHIMADZU. XPS was recorded using a Thermo Escalab 250. FESEM was conducted by a Hitachi S-4800. TEM was conducted by a Tecnai G220 transmission electron microscope. UV-vis absorption spectra and photoluminescence spectra were recorded by Hitachi U-4100 UV Spectrometer and Cary Eclipse Fluorescence Spectrophotometer, respectively. The Brunauer-Emmett-Teller (BET) was measured using a Quantachrome NOVA 2000e adsorption apparatus. The photoelectrochemical characterization was carried out on a Zennium electrochemical workstation. The electrolyte was 0.2 M Na<sub>2</sub>SO<sub>4</sub> aqueous solution. The generalized gradient approximation (GGA) with the Perdew-Burke-Ernzerhof (PBE) correction was adopted to calculate the work function using the CASTEP code.

## 3. Results and discussion

### 3.1. Structure and morphology

Fig. 1a illustrates the FT-IR spectra of the as-prepared samples. For the bare BiVO<sub>4</sub> sample, the sharp peak at 772 cm<sup>-1</sup> is attributed to the

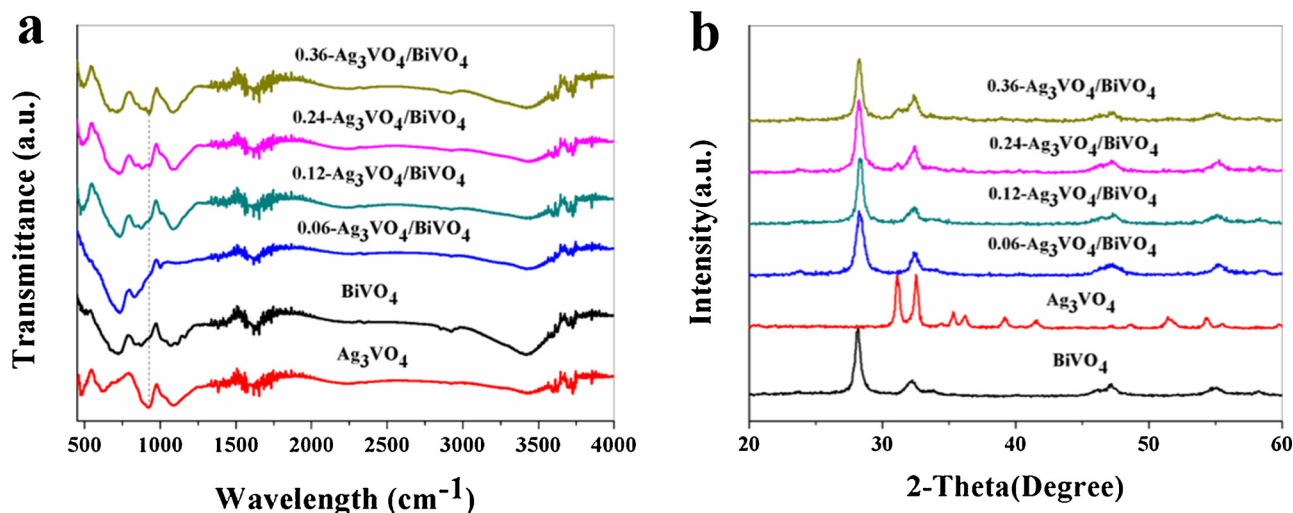


Fig. 1. (a) FT-IR spectra and (b) XRD patterns of the as-prepared samples.

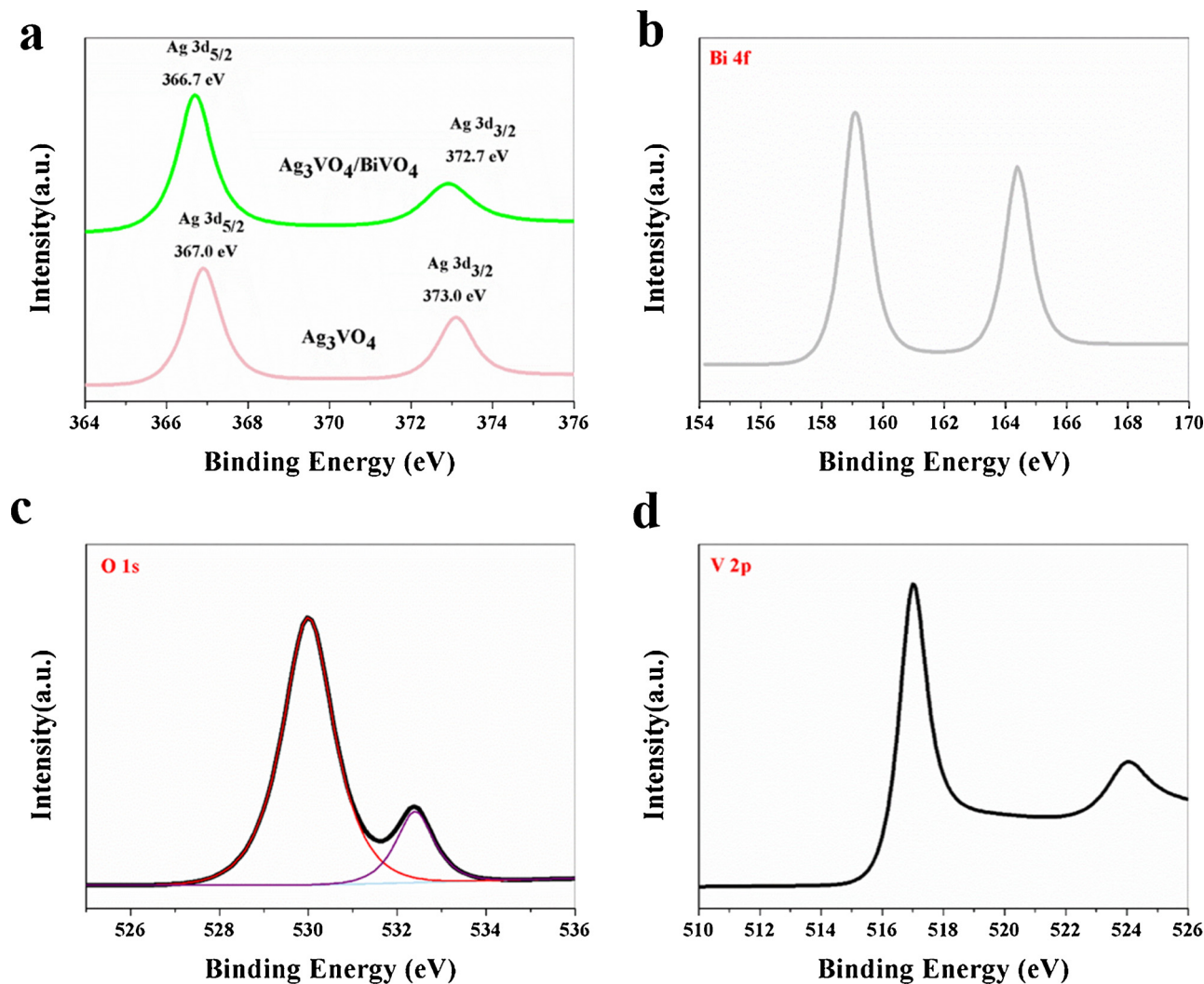
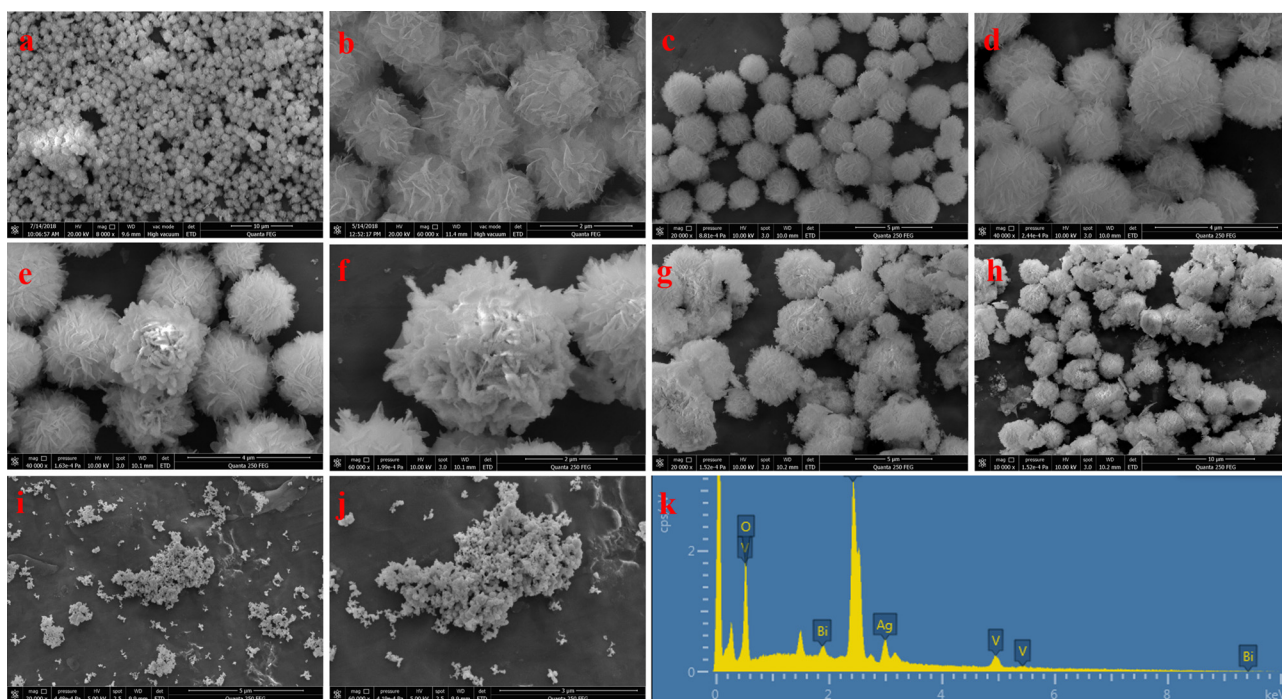


Fig. 2. (a) XPS spectra of Ag 3d, (b) XPS spectra of Bi 4f, (c) XPS spectra of O 1s, (d) XPS spectra of V 2p.

symmetrical stretching vibration of the Bi–O bond [66]. The peaks at 875 cm<sup>-1</sup> for the bare Ag<sub>3</sub>VO<sub>4</sub> sample can be assigned to the V=O double bond vibration [67], and this characteristic peak of Ag<sub>3</sub>VO<sub>4</sub> is also observed in the 0.24-Ag<sub>3</sub>VO<sub>4</sub>/BiVO<sub>4</sub>, which implied that the

Ag<sub>3</sub>VO<sub>4</sub> is successfully incorporated into the Ag<sub>3</sub>VO<sub>4</sub>/BiVO<sub>4</sub> sample. The XRD patterns of the samples were shown in Fig. 1b. It is clear that the samples are all monoclinic phase of BiVO<sub>4</sub> with body-centered structure [JCPDS: 14-0666]. The weak diffraction peak (32.4°) assigned





**Fig. 3.** (a–b) The FESEM image of  $\text{BiVO}_4$ , (c–d)  $0.12\text{-Ag}_3\text{VO}_4/\text{BiVO}_4$ , (e–f)  $0.24\text{-Ag}_3\text{VO}_4/\text{BiVO}_4$ , (g–h)  $0.36\text{-Ag}_3\text{VO}_4/\text{BiVO}_4$ , (i–j)  $\text{Ag}_3\text{VO}_4$ , (k) EDS spectrum of  $0.24\text{-Ag}_3\text{VO}_4/\text{BiVO}_4$ .

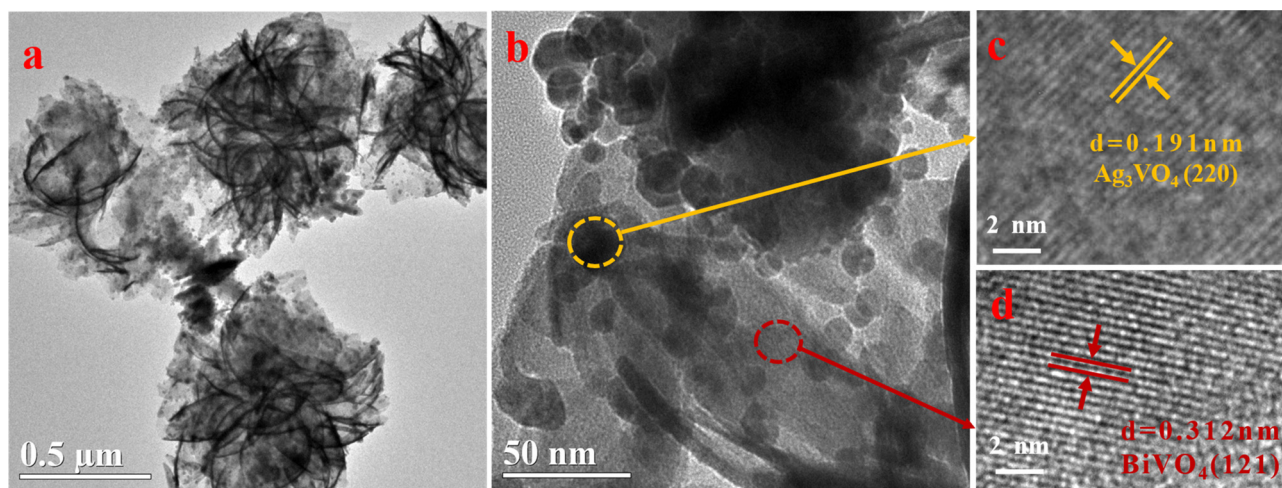


**Fig. 4.** (a–b) TEM image and (c–d) HRTEM image of  $0.24\text{-Ag}_3\text{VO}_4/\text{BiVO}_4$  photocatalyst.

to the (121) peak of  $\text{Ag}_3\text{VO}_4$  is found in the XRD patterns of the  $\text{Ag}_3\text{VO}_4/\text{BiVO}_4$  sample.

The binding energy of electric states and chemical bonds are analyzed by XPS in Fig. 2. For the Ag 3d (Fig. 2a), the Ag 3d peaks of  $\text{Ag}_3\text{VO}_4$  locate at 367.0 and 373.0 eV, which correspond to the Ag  $3d_{5/2}$  and Ag  $3d_{3/2}$  binding energies, respectively. However, the binding energies of Ag  $3d_{5/2}$  and Ag  $3d_{3/2}$  for the  $0.24\text{-Ag}_3\text{VO}_4/\text{BiVO}_4$  are 366.7 eV and 372.7 eV, respectively. Compared with the bare  $\text{BiVO}_4$ , the bands shift to lower binding energy in the Ag 3d spectra of the  $0.24\text{-Ag}_3\text{VO}_4/\text{BiVO}_4$ . This phenomenon may be mainly attributed to the changes in the local environment due to the depositing  $\text{Ag}_3\text{VO}_4$  on the  $\text{BiVO}_4$  sample, the  $\text{Ag}_3\text{VO}_4$  in the  $0.24\text{-Ag}_3\text{VO}_4/\text{BiVO}_4$  sample can work as an electron acceptor, thus electron can transfer from the  $\text{BiVO}_4$  to the  $\text{Ag}_3\text{VO}_4$ , thereby enhancing the charge density around  $\text{Ag}^+$ . Similar phenomena have also been reported by Zhu et al. [68]. From Fig. 2c, the predominant peak of O 1s (529.7 eV) is attributed to the lattice oxygen [69]. The other O 1s peaks can be belonged to the O

in  $\text{H}_2\text{O}$  (532.7 eV). The peaks located at 158.4, 164.1 and 516.8, 524.3 eV are consistent with  $\text{Bi}^{3+}$  and  $\text{V}^{5+}$  in Fig. 2b and d.

The morphologies of the photocatalysts were observed by FESEM and TEM. The  $\text{BiVO}_4$  microspheres with uniform flower-like structure were assembled by  $\text{BiVO}_4$  nanosheets (Fig. 3a and b). The  $\text{Ag}_3\text{VO}_4/\text{BiVO}_4$  with varying amounts of  $\text{Ag}_3\text{VO}_4$  are shown in Fig. 3c–h. Uniform deposition of  $\text{Ag}_3\text{VO}_4$  nanoparticles on the surface of  $\text{BiVO}_4$  are clearly evidenced. The EDS was preformed to confirms the elemental composition, it reveals that the  $0.24\text{-Ag}_3\text{VO}_4/\text{BiVO}_4$  sample contains bismuth, oxygen, vanadium, and silver elements (Fig. 3k).

We further verify that  $\text{Ag}_3\text{VO}_4$  nanoparticles are successfully loaded via the deposition process (Fig. 4a and b). As shown in the HRTEM image (Fig. 4c–d), the interplanar distances are 0.312, and 0.191 nm corresponding to the  $\text{BiVO}_4$  (121), and  $\text{Ag}_3\text{VO}_4$  (220) crystal plane, respectively [70,71]. Besides, the 2D-projected elemental mapping of  $\text{Ag}_3\text{VO}_4$  and  $0.24\text{-Ag}_3\text{VO}_4/\text{BiVO}_4$  samples disclose in Fig. 5, the pure  $\text{Ag}_3\text{VO}_4$  only possesses the elements of silver, oxygen, and vanadium.

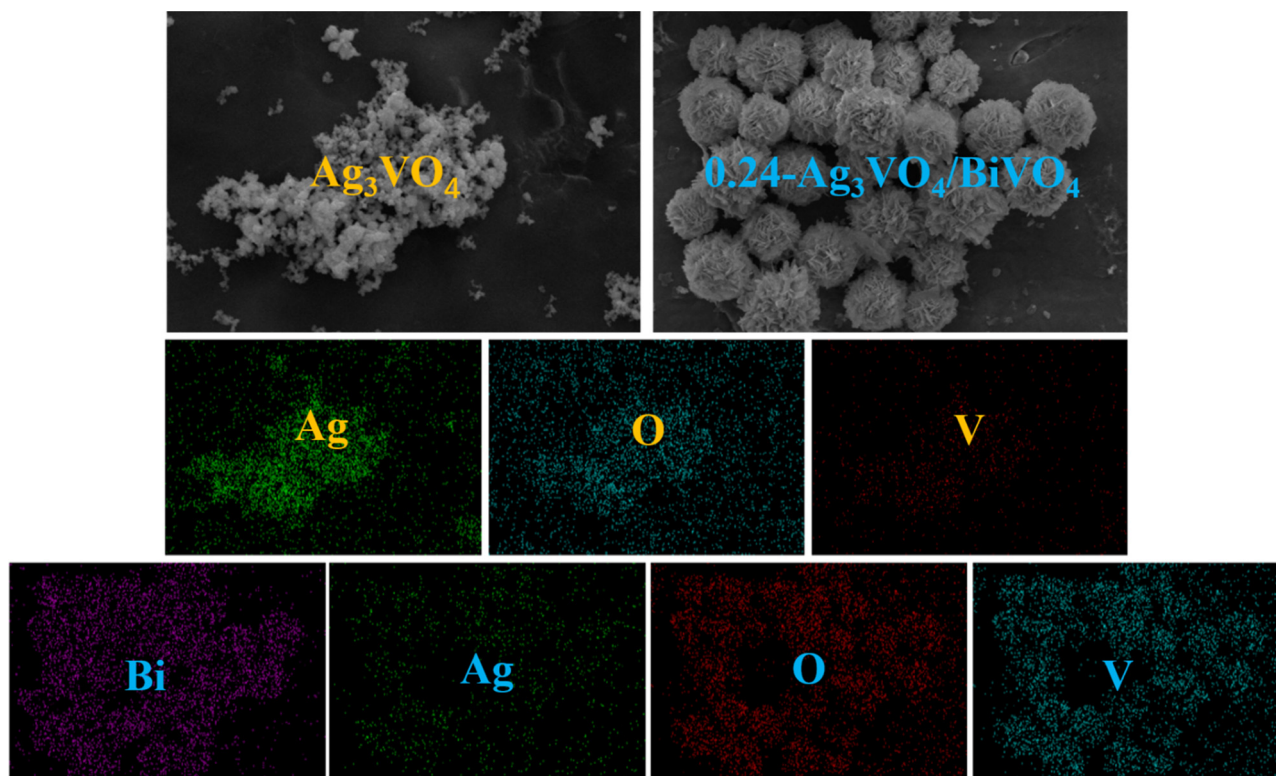


Fig. 5. SEM-EDS elemental mapping of  $\text{Ag}_3\text{VO}_4$  and  $0.24\text{-Ag}_3\text{VO}_4/\text{BiVO}_4$  photocatalyst.

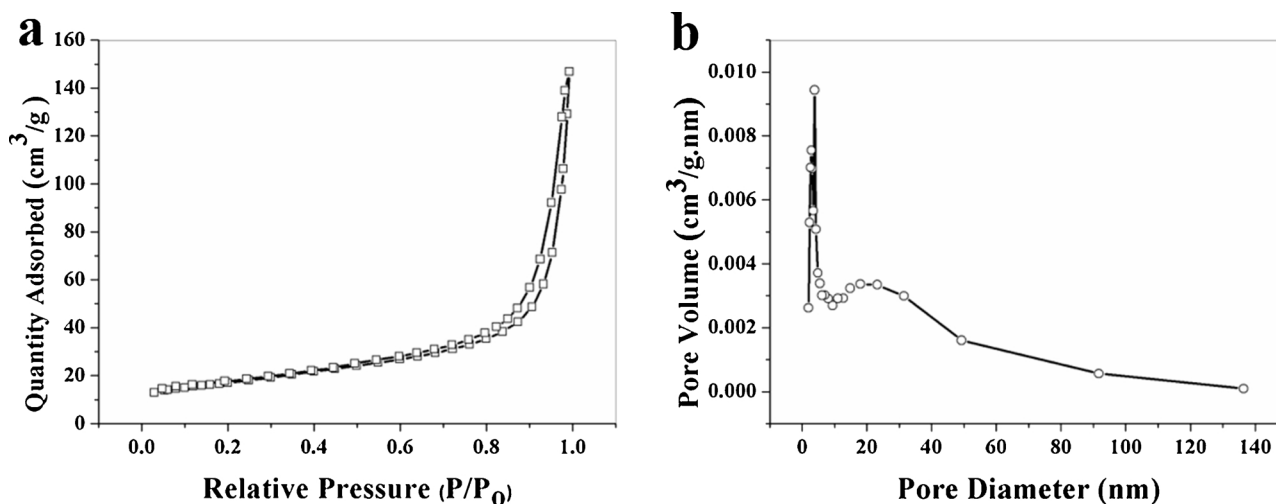


Fig. 6. (a) Nitrogen adsorption-desorption isotherm and (b) pore-size distribution for  $0.24\text{-Ag}_3\text{VO}_4/\text{BiVO}_4$  photocatalyst.

The  $0.24\text{-Ag}_3\text{VO}_4/\text{BiVO}_4$  sample contains the bismuth, oxygen, vanadium, and silver elements, which is also consistent with the result of EDS.

The results of BET and pore size distribution of the  $0.24\text{-Ag}_3\text{VO}_4/\text{BiVO}_4$  are shown in Fig. 6. The isotherms with a distinct hysteresis loop belong to type IV, indicating that the sample is meso-porous material. The specific surface area and the pore diameter of the sample are about  $39.01\text{ m}^2/\text{g}$  and  $16.28\text{ nm}$ , respectively. In addition, the specific surface area of the  $\text{BiVO}_4$  particles is  $5.41\text{ m}^2/\text{g}$  as shown in Fig. S2. As expected, its specific surface area is lower than that of the flower-like  $0.24\text{-Ag}_3\text{VO}_4/\text{BiVO}_4$  microspheres.

### 3.2. Optical properties

The UV-vis absorption spectra of the samples are shown in Fig. 7a. It is clear that the absorption edge of the  $\text{Ag}_3\text{VO}_4/\text{BiVO}_4$  shows a slight

red-shift with increasing of the loading amount of  $\text{Ag}_3\text{VO}_4$ . The band gap energy ( $E_g$ ) of the sample can be obtained by the Kubelka-Munk method [72]. As shown in Fig. 7b–d, the obtained value of  $E_g$  for  $\text{BiVO}_4$  and  $\text{Ag}_3\text{VO}_4$  are 2.50 and 2.20 eV, respectively. Whereas the  $E_g$  value of  $0.24\text{-Ag}_3\text{VO}_4/\text{BiVO}_4$  is about 2.44 eV, confirming that there are red-shift in the  $\text{Ag}_3\text{VO}_4/\text{BiVO}_4$  samples compared with the bare  $\text{BiVO}_4$ .

The PL spectra with the excited wavelength of 425 nm at room temperature were detected to investigate the carriers separated efficiency (Fig. 8a). The intensity of  $\text{Ag}_3\text{VO}_4/\text{BiVO}_4$  is weak compared with the bare  $\text{BiVO}_4$ , suggesting that efficient charge transfer exists between  $\text{Ag}_3\text{VO}_4$  and  $\text{BiVO}_4$ . The time-resolved fluorescence spectra further confirmed the efficient charge separation. It can be seen that the value of average lifetimes of the carriers ( $\tau_{\text{avg}}$ ) are 1.01 and 1.18 ns for the  $\text{BiVO}_4$  and  $0.24\text{-Ag}_3\text{VO}_4/\text{BiVO}_4$ , respectively (Fig. 8b and c). The increased  $\tau_{\text{avg}}$  indicates that forming heterojunction help prolong the



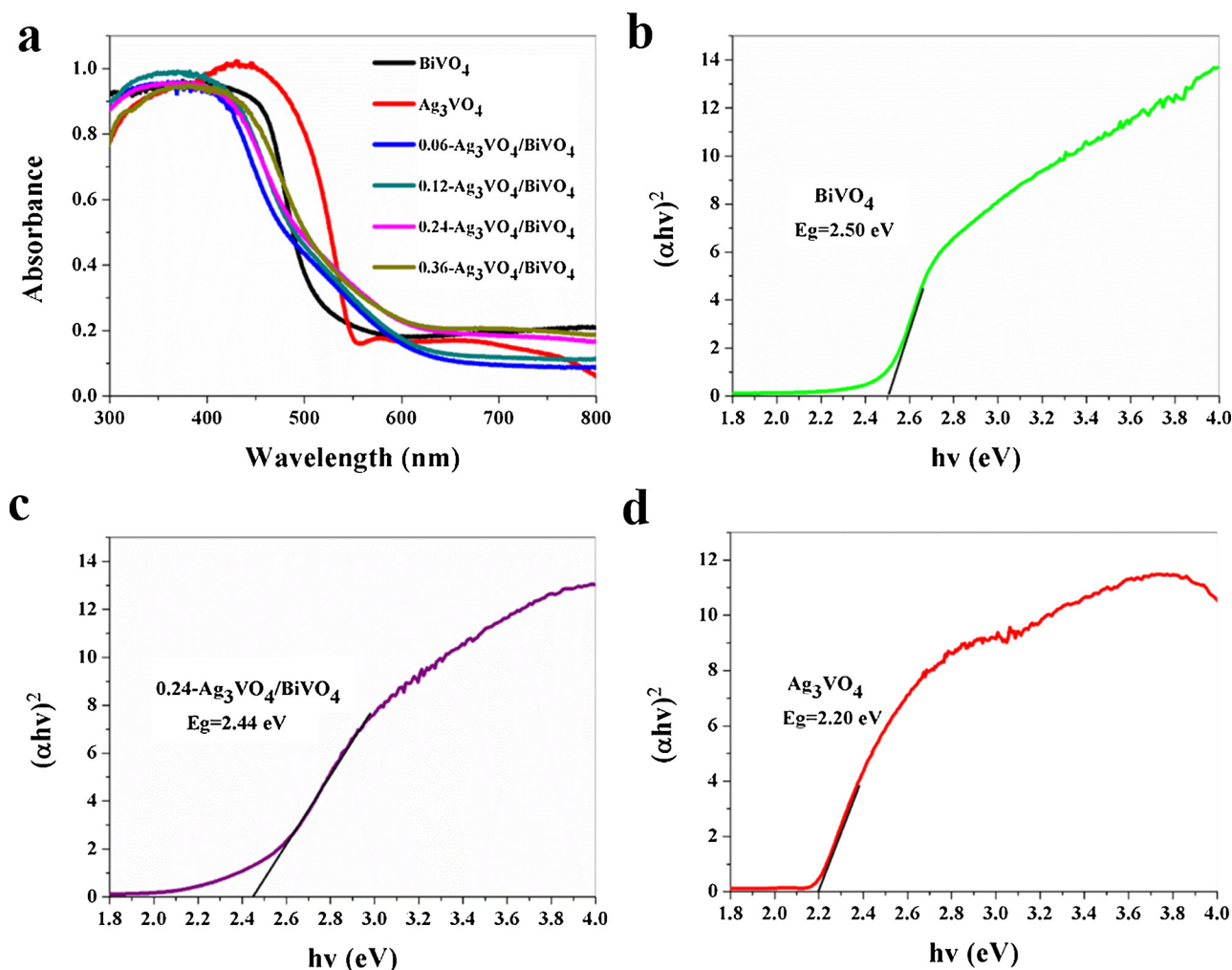


Fig. 7. (a) UV-vis absorption spectra of the as-prepared samples, (b–d) the plot of  $(\alpha h\nu)^2$  vs energy  $h\nu$  and band gap energy of the as-prepared samples.

photogenerated charge lifetime. The photoelectrochemical properties have been carried out to investigate carriers transport efficiency. As shown in Fig. 8d, it is clear that the photocurrent density of 0.24-Ag<sub>3</sub>VO<sub>4</sub>/BiVO<sub>4</sub> is the highest among these samples.

The  $N_D$  (carrier density) and  $E_{fb}$  (flat band potential) of the samples can be obtained by the Mott-Schottky (MS) Eq. (2):

$$1/C^2 = (2/q\epsilon\epsilon_0 N_D A^2) \cdot (E - E_{fb} - kT/q) \quad (2)$$

where  $C$  is the capacitance of space charge region,  $q$  is the electron charge,  $\epsilon$  is the dielectric constant,  $\epsilon_0$  is the permittivity of vacuum,  $N_D$  is the carrier density,  $A$  is the active area,  $E$  is applied bias potential,  $E_{fb}$  is the flat band potential,  $k$  is the Boltzmann constant and  $T$  is the absolute temperature [73]. As shown in Fig. 9a and b, the  $E_{fb}$  for the 0.24-Ag<sub>3</sub>VO<sub>4</sub>/BiVO<sub>4</sub> and BiVO<sub>4</sub> were  $-0.17$  V and  $-0.03$  V (vs. Ag/AgCl), respectively. The  $N_D$  was calculated from the slope of the linear region to be  $4.49 \times 10^{18}$  and  $5.61 \times 10^{18} \text{ cm}^{-3}$  for the bare BiVO<sub>4</sub> and 0.24-Ag<sub>3</sub>VO<sub>4</sub>/BiVO<sub>4</sub>, respectively. The higher donor density of 0.24-Ag<sub>3</sub>VO<sub>4</sub>/BiVO<sub>4</sub> than that of the bare BiVO<sub>4</sub> indicates that charge carrier transport was efficiently enhanced, confirming the formation of a heterojunction interface that acted as a sufficient space-charge layer in the Ag<sub>3</sub>VO<sub>4</sub>/BiVO<sub>4</sub> sample. Electrochemical impedance spectroscopy (EIS) measurements were displayed in the Fig. 9c. Compared with the bare BiVO<sub>4</sub>, the 0.24-Ag<sub>3</sub>VO<sub>4</sub>/BiVO<sub>4</sub> sample exhibits smaller charge transfer resistance, indicating that it possesses excellent performance in the charge-transfer process [74]. The results of the above these characterizations suggest that Ag<sub>3</sub>VO<sub>4</sub>/BiVO<sub>4</sub> possesses excellent separation efficiency of photogenerated electron-hole pairs.

### 3.3. Photocatalytic activity

Fig. 10a shows the photocatalytic reduction of Cr<sup>6+</sup> and oxidation of BPS over different samples. A dark adsorption experiment was also operated in order to achieve an equilibrium adsorption state. The BiVO<sub>4</sub> particles displayed lower photocatalytic activities than that of the flower-like BiVO<sub>4</sub> microspheres, which can be ascribed to its relatively small specific surface area as mentioned (BET 5.4 m<sup>2</sup>/g). The photocatalytic performance of Ag<sub>3</sub>VO<sub>4</sub>/BiVO<sub>4</sub> is higher than those of BiVO<sub>4</sub> and Ag<sub>3</sub>VO<sub>4</sub>. Among the as-prepared Ag<sub>3</sub>VO<sub>4</sub>/BiVO<sub>4</sub> with various Ag<sub>3</sub>VO<sub>4</sub> contents, 0.24-Ag<sub>3</sub>VO<sub>4</sub>/BiVO<sub>4</sub> exhibits the highest photocatalytic performances. The photocatalytic reduction and oxidation efficiency of 0.24-Ag<sub>3</sub>VO<sub>4</sub>/BiVO<sub>4</sub> can achieve 74.9 and 94.8%, respectively, after 150 min visible-light irradiation. The results show that there is an optimal depositing amount of Ag<sub>3</sub>VO<sub>4</sub> nanoparticles on the BiVO<sub>4</sub> surface for the enhancement of photocatalytic performances. It is proposed that if the amount of Ag<sub>3</sub>VO<sub>4</sub> is too low, the trapping sites of carriers increase with increasing the Ag<sub>3</sub>VO<sub>4</sub> deposition amount, which prolongs the lifetime of carriers, hence improving the photocatalytic activity. On the contrary, if the deposition amount of Ag<sub>3</sub>VO<sub>4</sub> is too high, excessive loading of Ag<sub>3</sub>VO<sub>4</sub> may block photogenerated electrons transfer and hence reduce active site exposure because of high overlapping Ag<sub>3</sub>VO<sub>4</sub> particles with each other. Moreover, on the basis of the observed photocatalytic activities, the QE for the photocatalytic reduction of Cr<sup>6+</sup> was calculated. The QE for the 0.24-Ag<sub>3</sub>VO<sub>4</sub>/BiVO<sub>4</sub> sample was 28.80%, this QE is much higher than that of the bare Ag<sub>3</sub>VO<sub>4</sub> (QE = 8.38%) and BiVO<sub>4</sub> (QE = 11.04%) samples under

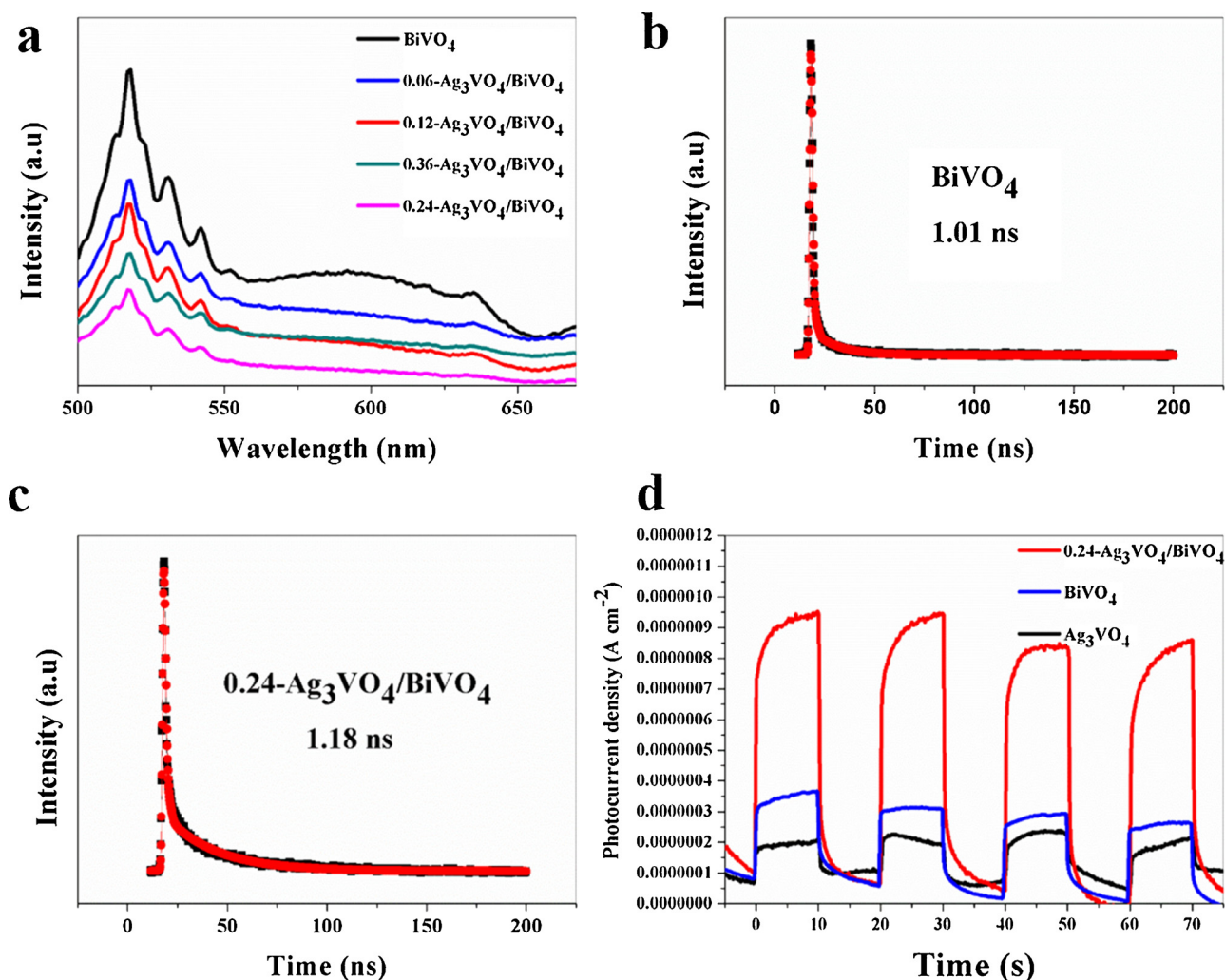


Fig. 8. (a) PL spectra of the as-prepared samples, (b) fluorescence emission decay curves of the BiVO<sub>4</sub>, (c) fluorescence emission decay curves of the 0.24-Ag<sub>3</sub>VO<sub>4</sub>/BiVO<sub>4</sub>, (d) photocurrent of the as-prepared samples.

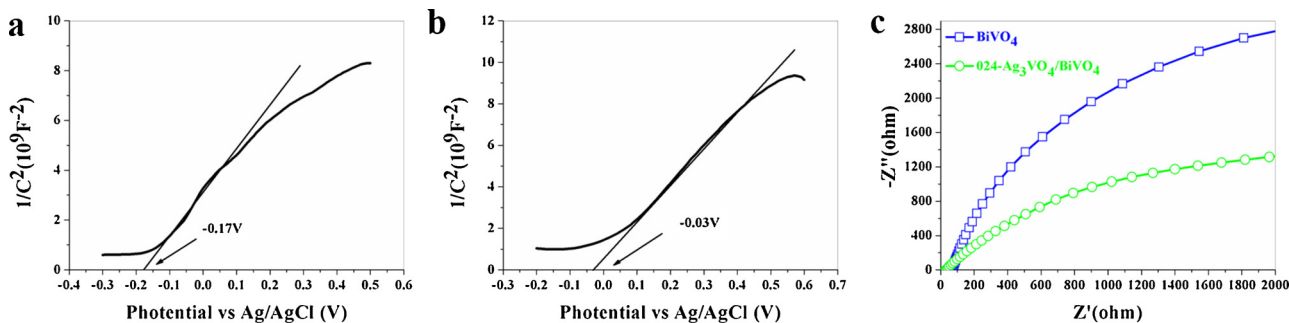
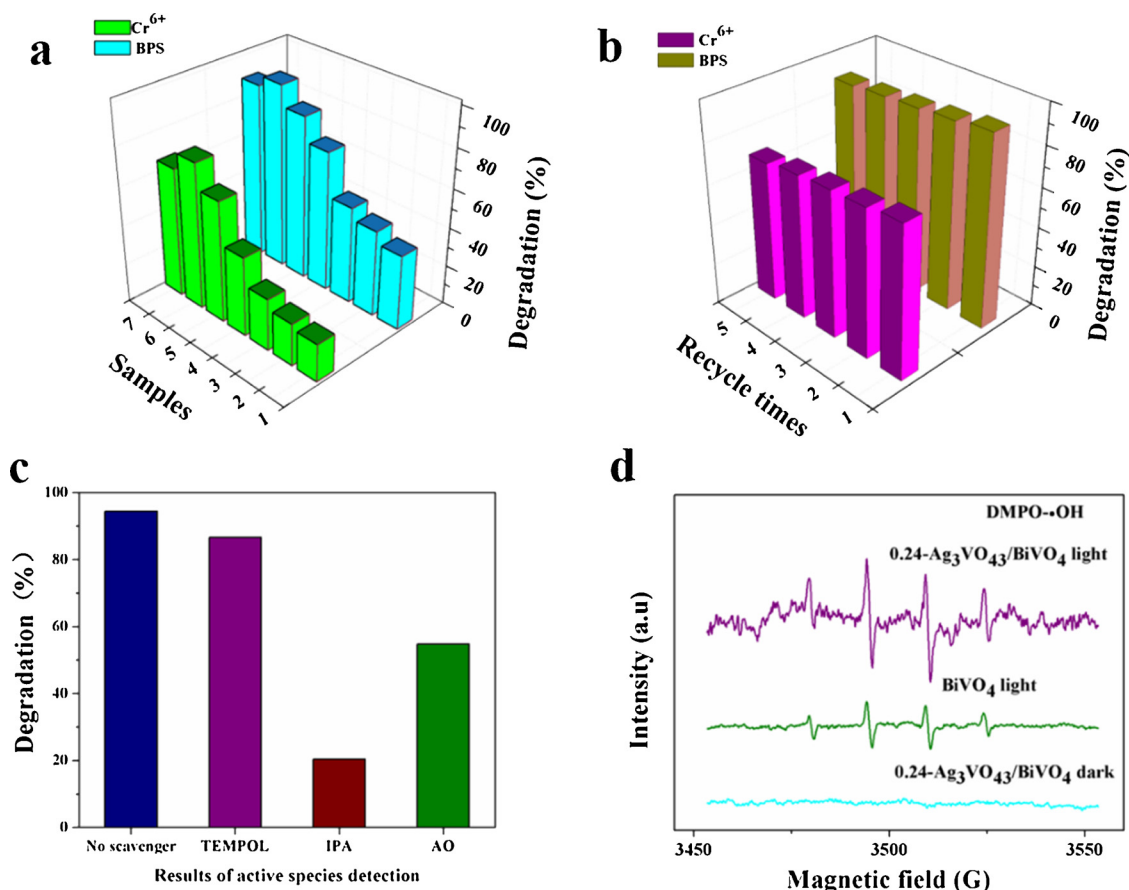


Fig. 9. Mott-Schottky plot of (a) 0.24-Ag<sub>3</sub>VO<sub>4</sub>/BiVO<sub>4</sub> and (b) bare BiVO<sub>4</sub>; (c) Nyquist plot of electrochemical impedance spectroscopy of the samples.

visible-light irradiation.

The photocatalytic activity of stability for the Ag<sub>3</sub>VO<sub>4</sub>/BiVO<sub>4</sub> was studied (Fig. 10b). Clearly, the result shows that the sample has adequate stability. To check for the reactive species involved in the photocatalytic reaction, 4-Hydroxy-TEMPO (TEMPOL), isopropanol (IPA) and oxalic acid (AO) were used to quench  $\cdot\text{O}_2^-$ ,  $\cdot\text{OH}$  and  $\text{h}^+$ , respectively, [75–77]. As shown in Fig. 10c, the roles of  $\cdot\text{O}_2^-$  was verified to be insignificant compared with those of  $\cdot\text{OH}$  and  $\text{h}^+$  in the active species trapping experiment, indicating that  $\cdot\text{OH}$  and  $\text{h}^+$  were the predominant active species in this reaction system. The presence of  $\cdot\text{OH}$  radicals was also confirmed by the EPR technique with DMPO, as

shown in Fig. 10d. The signal (peaks intensity = 1:2:2:1) of the DMPO- $\cdot\text{OH}$  was found under the visible light irradiation. However, the  $\cdot\text{OH}$  signal cannot be observed without light irradiation. In addition, compared with the spectrum for the 0.24-Ag<sub>3</sub>VO<sub>4</sub>/BiVO<sub>4</sub> and BiVO<sub>4</sub> under the light irradiation, the former intensity was higher than the latter, which suggests that heterojunction structure improve separation efficiency of photogenerated carriers and favour the formation of  $\cdot\text{OH}$  radicals.



**Fig. 10.** (a) Photocatalytic activities of the as-prepared photocatalysts for Cr<sup>6+</sup> and BPS degradation, sample 1: BiVO<sub>4</sub> particles, sample 2: Ag<sub>3</sub>VO<sub>4</sub>, sample 3: BiVO<sub>4</sub> microspheres, sample 4: 0.06-Ag<sub>3</sub>VO<sub>4</sub>/BiVO<sub>4</sub>, sample 5: 0.12-Ag<sub>3</sub>VO<sub>4</sub>/BiVO<sub>4</sub>, sample 6: 0.24-Ag<sub>3</sub>VO<sub>4</sub>/BiVO<sub>4</sub>, sample 7: 0.36-Ag<sub>3</sub>VO<sub>4</sub>/BiVO<sub>4</sub>, (b) recycling runs of Cr<sup>6+</sup> and BPS degradation, (c) the effect of different quenchers on the photocatalytic degradation of BPS, and (d) spin-trapping EPR spectra.

### 3.4. Photocatalysis mechanism

In order to further disclose the energy band structure of the photocatalysts, the calculation using density functional theory (DFT) and exploration of the valence band XPS (VB-XPS) spectra were carried out. Two theoretical structure models of the Ag<sub>3</sub>VO<sub>4</sub> and BiVO<sub>4</sub> were used, as shown in Fig. 11. It is clear that Eg for the Ag<sub>3</sub>VO<sub>4</sub> and BiVO<sub>4</sub> are 2.12, and 2.54 eV, respectively.

Fig. 12a and b show the valence band XPS (VB-XPS) spectra near the Fermi level. By extrapolating the leading edge of the VB to its intersection with background counts near the Fermi level, the position of the Fermi level with respect to the VB maximum (VBM) could be determined. The Fermi level is located at 2.10 eV above the VBM for the BiVO<sub>4</sub>, whereas it is 1.75 eV for the Ag<sub>3</sub>VO<sub>4</sub>.

Furthermore, the Fermi level can be obtained via CASTEP code, which were shown in Fig. 13. The positions of the Fermi level of BiVO<sub>4</sub> and Ag<sub>3</sub>VO<sub>4</sub> are located at -5.17 and -4.98 eV/AVS, respectively. According to the positions of the Fermi level of them and combined with the results derived from VB-XPS, the VB edge levels of the BiVO<sub>4</sub> and Ag<sub>3</sub>VO<sub>4</sub> are -7.27 and -6.73 eV/AVS (2.77 eV, 2.23 eV/NHE) respectively. In addition, according to the results of simulation and experiments as shown in Figs. 7 and 11, Eg value of 2.50 and 2.20 eV for the BiVO<sub>4</sub> and Ag<sub>3</sub>VO<sub>4</sub> were adopted, respectively. Thus, the CB edge levels of the BiVO<sub>4</sub> and Ag<sub>3</sub>VO<sub>4</sub> are -4.77 and -4.53 eV/AVS (0.27 eV, 0.03 eV/NHE), respectively.

On the basis of the band positions result, a tentatively probable mechanism for the visible light photocatalysis of the heterojunction is proposed, as shown in Fig. 14. If Ag<sub>3</sub>VO<sub>4</sub> and BiVO<sub>4</sub> can form a conventional electron-hole separation process, the electron formed in the

Ag<sub>3</sub>VO<sub>4</sub> conduction band can transfer to the conduction band of BiVO<sub>4</sub>. Conversely, the hole can transfer from the valence band of BiVO<sub>4</sub> to the valence band of Ag<sub>3</sub>VO<sub>4</sub>. Consequently, the heterojunction forms a type-II staggered band alignment, which favors the separation of charge carriers. However, the valence band potential of 2.23 eV/NHE (-6.73 eV/AVS) for Ag<sub>3</sub>VO<sub>4</sub> is lower compared to the H<sub>2</sub>O/HO<sup>•</sup> redox potential (2.68 eV/NHE, -7.18 eV/AVS) [78], indicating that the photoinduced holes accumulated in the valence band of Ag<sub>3</sub>VO<sub>4</sub> cannot efficiently oxidize the adsorbed H<sub>2</sub>O to form HO<sup>•</sup> radical. Thus, the formation of HO<sup>•</sup> reactive species is not favorable in such a situation, which is inconsistent with the results of the free radical scavenging activity and EPR tests, this illustrated that the proposal mechanism of type-II staggered band alignment presents some limitations in this system. In addition, the photoinduced redox probe reactions, Au<sup>3+</sup> + e<sup>-</sup> → Au and Mn<sup>2+</sup> + h<sup>+</sup> + OH<sup>-</sup> → MnO<sub>x</sub>, verify the Z-scheme electron transfer on the Ag<sub>3</sub>VO<sub>4</sub>/BiVO<sub>4</sub> sample under visible light. The Au particles are clearly deposited on the surface of Ag<sub>3</sub>VO<sub>4</sub> particles (Fig. S4a). For the photooxidation deposition of MnO<sub>x</sub>, the rod-like MnO<sub>x</sub> particles are large, but carefully observed, it can be seen that the MnO<sub>x</sub> particles are deposited on the surface of BiVO<sub>4</sub> (Fig. S4b). This result verifies that Ag<sub>3</sub>VO<sub>4</sub> mainly serves as active sites of photocatalytic reduction while BiVO<sub>4</sub> as the photocatalytic oxidation sites. The Z-scheme model is also favorable for the photogenerated charge separation, which was understood by PL spectra photocurrent (Fig. 8a), time-resolved fluorescence spectra (Fig. 8c), photocurrent measure (Fig. 8d), Mott-Schottky plot (Fig. 9a), and Nyquist plot of electrochemical impedance spectroscopy (Fig. 9c) of the Ag<sub>3</sub>VO<sub>4</sub>/BiVO<sub>4</sub> sample.

Based on the above discussion, the Ag<sub>3</sub>VO<sub>4</sub>/BiVO<sub>4</sub> heterostructures



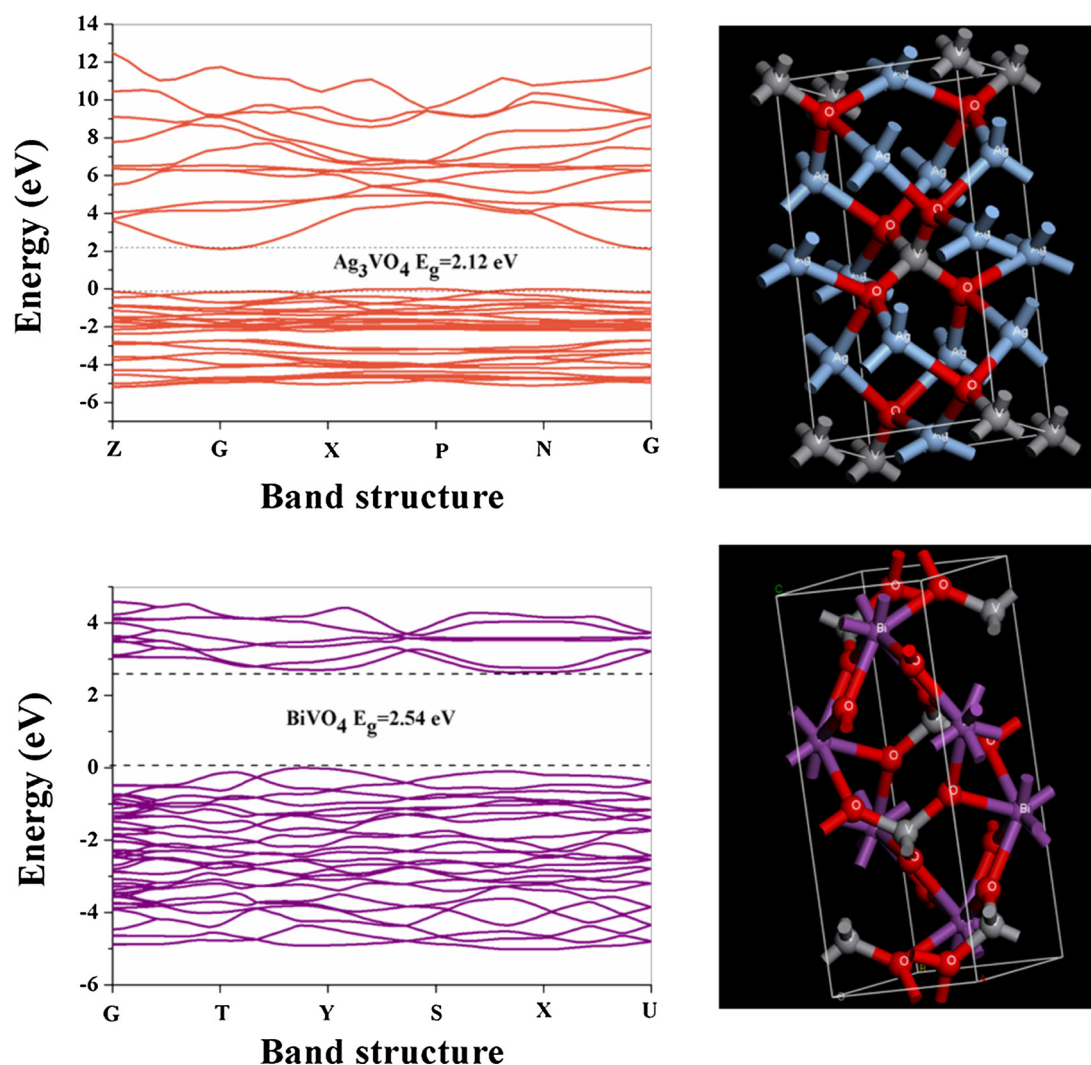


Fig. 11. Calculated band structures (left) and crystal structures (right) of the samples.

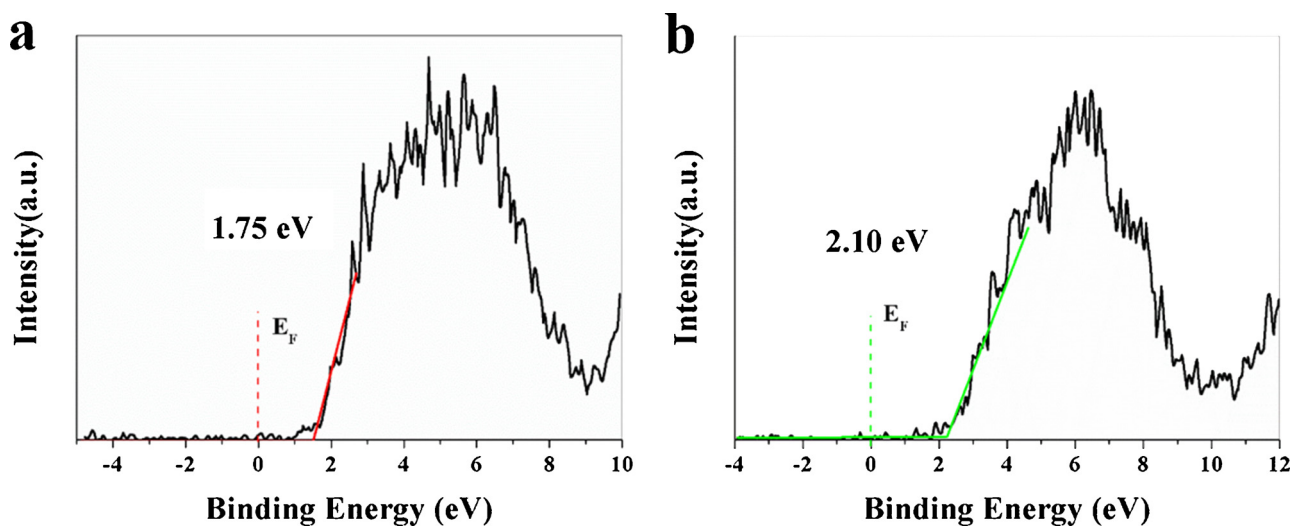


Fig. 12. VB-XPS spectra of the (a)  $\text{Ag}_3\text{VO}_4$  and (b)  $\text{BiVO}_4$  samples. The Fermi level  $E_F$  is located at  $E = 0$  eV, as marked by the vertical dot line.

may follow a typical Z-scheme charge transfer system, as shown in Fig. 15. In the direct Z-scheme charge transfer mechanism, the photo-induced conduction band electrons of the  $\text{BiVO}_4$  transfer to the valence band of the  $\text{Ag}_3\text{VO}_4$ . The more positive VB potential of  $\text{BiVO}_4$  (2.77 eV/

NHE) compared to the  $\text{H}_2\text{O}/\text{HO}^\cdot$  potential can oxidize the  $\text{H}_2\text{O}$  into  $\text{HO}^\cdot$  radicals, which is more conducive to the production of  $\text{HO}^\cdot$  radicals, verifying by EPR test. Moreover, the Fermi level of the  $\text{Ag}_3\text{VO}_4$  is higher compared to that of  $\text{BiVO}_4$ , the electrons will flow from  $\text{Ag}_3\text{VO}_4$  to

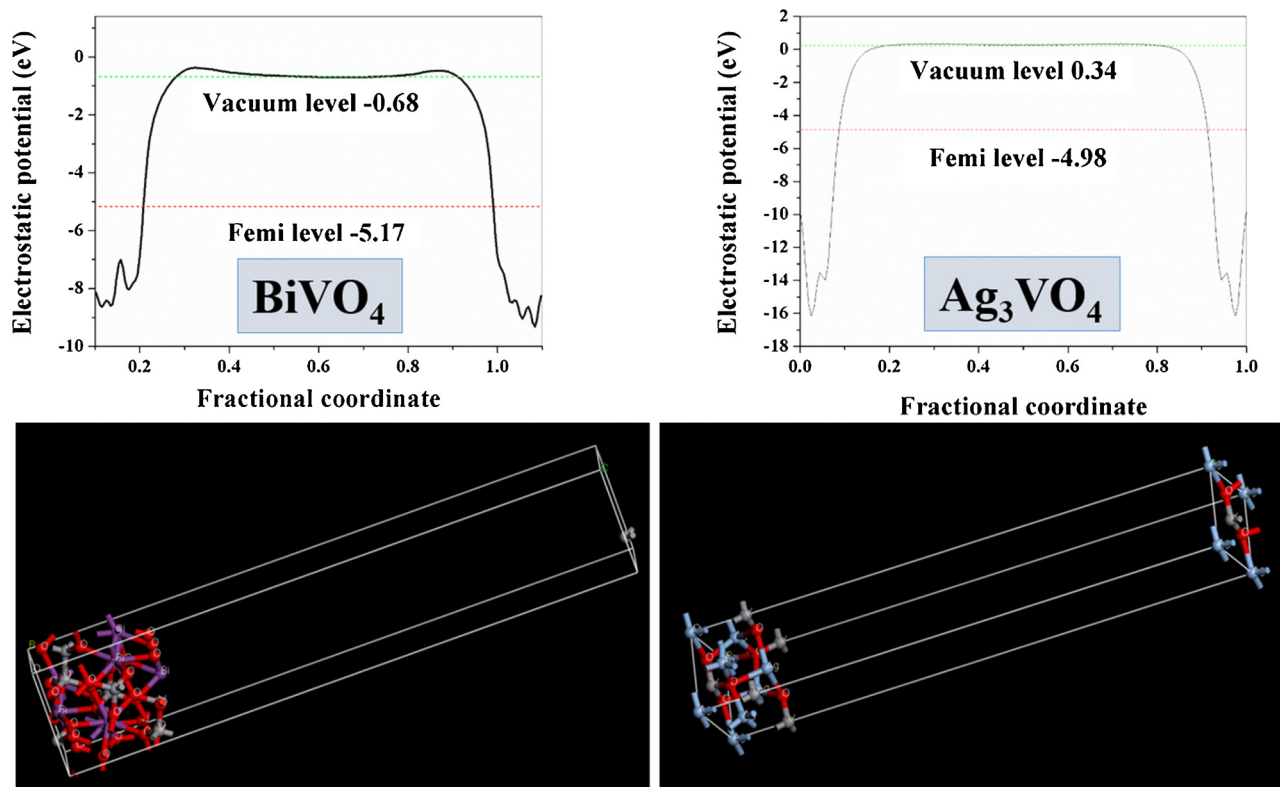


Fig. 13. The crystal structure and work function of  $\text{BiVO}_4$  (121) and  $\text{Ag}_3\text{VO}_4$  (220).

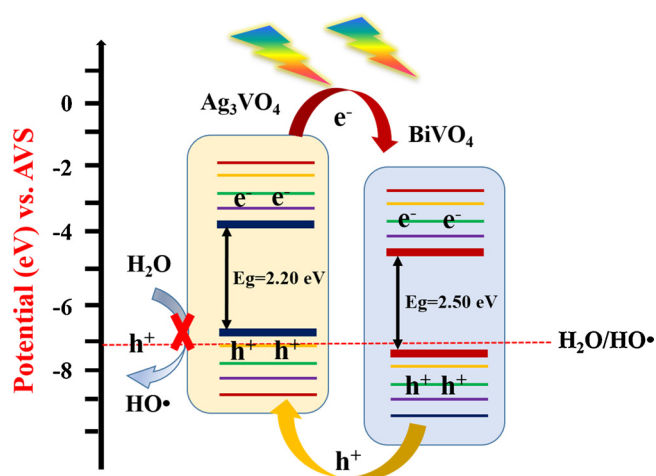


Fig. 14. The proposed type-II staggered band alignment of  $\text{Ag}_3\text{VO}_4/\text{BiVO}_4$  photocatalyst.

$\text{BiVO}_4$ . The Fermi level of  $\text{Ag}_3\text{VO}_4$  is downward, while that of  $\text{BiVO}_4$  are upward until the equilibrium is obtained under the circumstances. Due to the electron transfer, a built-in electric field ( $E$ ) directed from  $\text{Ag}_3\text{VO}_4$  to  $\text{BiVO}_4$  surface will be established when an equalized Fermi level is reached by the two components. Furthermore, the existence of interfacial built-in potential is beneficial to the separation of photo-generated charge carriers in the way of Z-scheme charges transfer mechanism, thereby inhibiting their recombination rate to improve the photocatalytic activity of the heterostructures.

#### 4. Conclusions

A novel Z-scheme  $\text{Ag}_3\text{VO}_4/\text{BiVO}_4$  heterojunction photocatalyst was successfully obtained, the photocatalytic performance of the as-

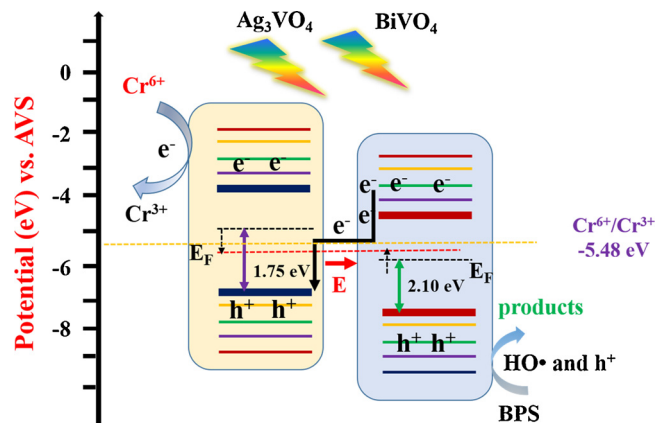


Fig. 15. The photocatalysis enhancement mechanism of the Z-scheme  $\text{Ag}_3\text{VO}_4/\text{BiVO}_4$  photocatalyst.

prepared photocatalyst was systematically examined via the photocatalytic reduction of  $\text{Cr}^{6+}$  and oxidation of BPS organic compounds under visible-light irradiation. Among these samples, 0.24- $\text{Ag}_3\text{VO}_4/\text{BiVO}_4$  exhibits the highest photocatalytic performances, the photocatalytic reduction and oxidation efficiency can achieve 74.9 and 94.8%, respectively. The enhancing photocatalytic performance is attributed to the build in electric field assisted charge transfer between the  $\text{Ag}_3\text{VO}_4$  and  $\text{BiVO}_4$ , and the increasing lifetime of the charge carrier confirmed by the results of time-resolved fluorescence spectra and photoelectrochemical measures. Moreover, based on the results of experiments and simulations, the  $\text{Ag}_3\text{VO}_4/\text{BiVO}_4$  heterostructures follow a typical Z-scheme charge transfer mechanism rather than a conventional type-II heterojunction charge transfer mechanism.

## Acknowledgements

We greatly acknowledge the National Natural Science Foundation of China (51808250, 51472101), the Natural Science Foundation of Jiangsu Province of China (BK20181070, BK20160430), the China Postdoctoral Science Foundation (2017M610336, 2016M591757), the Natural Science Foundation of Jiangsu Provincial Department of Education (17KJA150002), the Jiangsu Planned Projects for Postdoctoral Research Funds (1601179C), Huaian Natural Science Research Program (HAB201830), the Key University Science Research Project of Jiangsu Province (11KJA150004), the Shanghai Tongji Gao Tingyao Environmental Science & Technology Development Foundation (STGEF), and the Hong Kong Scholars Program 2017.

## Appendix A. Supplementary data

Supplementary material related to this article can be found, in the online version, at doi:<https://doi.org/10.1016/j.apcatb.2019.01.001>.

## References

- [1] Y.W. Feng, H. Li, L.L. Ling, S. Yan, D.L. Pan, H. Ge, H.X. Li, Z.F. Bian, *Environ. Sci. Technol.* 52 (2018) 7842–7848.
- [2] T.W. Kim, K.S. Choi, *Science* (2014) 1245026.
- [3] H. Ullah, A.A. Tahir, T.K. Mallick, *Appl. Catal. B* 224 (2018) 895–903.
- [4] J. Low, J. Yu, M. Jaroniec, S. Wageh, A.A. Al-Ghamdi, *Adv. Mater.* 29 (2017) 1601694.
- [5] J.M. Wu, Y. Chen, L. Pan, P.H. Wang, Y. Cui, D.C. Kong, L. Wang, X.W. Zhang, J.J. Zou, *Appl. Catal. B* 221 (2018) 187–195.
- [6] Y. Ye, Z. Zang, T. Zhou, F. Dong, S. Lu, X. Tang, W. Wei, Y. Zhang, *J. Catal.* 357 (2018) 100–107.
- [7] P. Fernández-Ibáñez, M.I. Polo-López, S. Malato, S. Wadhwa, J.W.J. Hamilton, P.S.M. Dunlop, R. D'Sa, E. Magee, K. O'Shea, D.D. Dionysiou, J.A. Byrne, *Chem. Eng. J.* 261 (2015) 36–44.
- [8] G. Zhang, Y. Zhang, M. Nadagouda, C. Han, K. O'Shea, S.M. El-Sheikh, A.A. Ismail, D.D. Dionysiou, *Appl. Catal. B* 144 (2014) 614–621.
- [9] C. Belver, J. Bedia, M.A. Álvarez-Montero, J.J. Rodríguez, *Catal. Today* 266 (2016) 36–45.
- [10] Y. Kanigridou, A. Petala, Z. Frontistis, M. Antonopoulou, M. Solakidou, I. Konstantinou, Y. Deligiannakis, D. Mantzavinos, D.I. Kondarides, *Chem. Eng. J.* 318 (2017) 39–49.
- [11] Y. Gong, X. Quan, H. Yu, S. Chen, *Appl. Catal. B* 219 (2017) 439–449.
- [12] G.N. Nomikos, P. Panagiotopoulou, D.I. Kondarides, X.E. Verykios, *Appl. Catal. B* 146 (2014) 249–257.
- [13] J. Zhang, L. Zhang, Y. Shi, G. Xu, E. Zhang, H. Wang, Z. Kong, J. Xi, Z. Ji, *Appl. Surf. Sci.* 420 (2017) 839–848.
- [14] O. Sacco, V. Vaiano, C. Han, D. Sannino, D.D. Dionysiou, *Appl. Catal. B* (2015) 462–474.
- [15] Y. Li, F.T. Liu, Y. Chang, J. Wang, C.W. Wang, *Appl. Surf. Sci.* 426 (2017) 770–780.
- [16] Y. Zhang, C. Han, M.N. Nadagouda, D.D. Dionysiou, *Appl. Catal. B* 168 (2015) 550–558.
- [17] C. Belver, C. Han, J.J. Rodríguez, D.D. Dionysiou, *Catal. Today* 280 (2017) 21–28.
- [18] C. Belver, J. Bedia, J.J. Rodríguez, *Appl. Catal. B* 176 (2015) 278–287.
- [19] Y.M. Xie, L. Lv, M.H. Li, B.C. Pan, Q. Chen, W.M. Zhang, Q.X. Zhang, *Sci. China Chem.* 55 (2012) 409–415.
- [20] H. Li, H. Yu, X. Quan, S. Chen, H. Zhao, *Adv. Fun. Mater.* 25 (2015) 3074–3080.
- [21] M. Tobajas, C. Belver, J.J. Rodríguez, *Chem. Eng. J.* 309 (2017) 596–606.
- [22] H. Zhao, H. Yu, X. Quan, S. Chen, Y. Zhang, H. Zhao, H. Wang, *Appl. Catal. B* 152 (2014) 46–50.
- [23] E. Ioannidou, Z. Frontistis, M. Antonopoulou, D. Venieri, I. Konstantinou, D.I. Kondarides, D. Mantzavinos, *Chem. Eng. J.* 318 (2017) 143–152.
- [24] H. Yu, L. Song, Y. Hao, N. Lu, X. Quan, S. Chen, Y. Zhang, Y. Feng, *Chem. Eng. J.* 283 (2016) 1506–1513.
- [25] C.F. Mu, Y. Zhang, W.Q. Cui, Y.H. Liang, Y.F. Zhu, *Appl. Catal. B* 212 (2017) 41–49.
- [26] Y.W. Feng, L.L. Ling, Y.X. Wang, Z.M. Xu, F.L. Cao, H.X. Li, Z.F. Bian, *Nano Energy* 40 (2017) 481–486.
- [27] H. Li, X. Quan, S. Chen, H. Yu, *Appl. Catal. B* 209 (2017) 591–599.
- [28] K.F. Zhang, Y.X. Liu, J.G. Deng, S.H. Xie, H.X. Lin, X.T. Zhao, J. Yang, Z. Han, H.X. Dai, *Appl. Catal. B* 202 (2017) 569–579.
- [29] X. Li, J. Wang, Y. Men, Z. Bian, *Appl. Catal. B* 187 (2016) 115–121.
- [30] J.G. Yu, J.X. Low, W. Xiao, P. Zhou, M. Jaroniec, *J. Am. Chem. Soc.* 136 (2014) 8839–8842.
- [31] L. Liu, L. Ding, Y.G. Liu, W.J. An, S.L. Lin, Y.H. Liang, W.Q. Cui, *Appl. Catal. B* 201 (2017) 92–104.
- [32] S.W. Cao, Y. Li, B.C. Zhu, M. Jaroniec, J.G. Yu, *J. Catal.* 349 (2017) 208–217.
- [33] F.Y. Chen, W.J. An, L. Liu, Y.H. Liang, W.Q. Cui, *Appl. Catal. B* 217 (2017) 65–80.
- [34] Y. Feng, L. Ling, J. Nie, K. Han, X. Chen, Z. Bian, H.L.Z.L. Wang, *ACS Nano* 11 (2017) 12411–12418.
- [35] Z.K. He, J.W. Fu, B. Cheng, J.G. Yu, S.W. Cao, *Appl. Catal. B* 205 (2017) 104–111.
- [36] X. Chen, L. Liu, Y. Feng, L. Wang, Z. Bian, H. Li, Z.L. Wang, *Mater. Today* 20 (2017) 501–506.
- [37] W. Zhao, B. Dai, F. Zhu, X. Tu, J. Xu, L. Zhang, S. Li, D.Y.C. Leung, C. Sun, *Appl. Catal. B* 229 (2018) 171–180.
- [38] S. Song, H. Yang, C. Zhou, J. Cheng, Z. Jiang, Z. Lu, J. Miao, *Chem. Eng. J.* 320 (2017) 342–351.
- [39] F.Q. Zhou, J.C. Fan, Q.J. Xu, Y.L. Min, *Appl. Catal. B* 201 (2017) 77–83.
- [40] Q. Wang, J. He, Y. Shi, S. Zhang, T. Niu, H. She, Y. Bi, *Chem. Eng. J.* 326 (2017) 411–418.
- [41] L. Chen, R. Huang, Y.J. Ma, S.L. Luo, C.T. Au, S.F. Yin, *RSC Adv.* 3 (2013) 24354–24361.
- [42] M.W. Kim, K. Kim, T.Y. Ohm, H. Yoon, B. Joshi, E. Samuel, M.T. Swihart, S. KyuChoi, H. Park, S.S. Yoon, *Chem. Eng. J.* 333 (2018) 721–729.
- [43] L. Chen, Q. Zhang, R. Huang, S.F. Yin, S.L. Luo, C.T. Au, *Dalton Trans.* 41 (2012) 9513–9518.
- [44] C. Liu, Y. Yang, J. Li, S. Chen, W. Li, X. Tang, *Chem. Eng. J.* 326 (2017) 603–611.
- [45] S. Singh, R. Sharma, B. RajMehta, *Appl. Surf. Sci.* 411 (2017) 321–330.
- [46] C. Wu, Y. Fang, A.H. Tirusew, M. Xiang, Y. Huang, C. Chen, *Chin. J. Catal.* 38 (2017) 192–198.
- [47] X. Song, Y. Li, Z. Wei, S. Ye, D.D. Dionysiou, *Chem. Eng. J.* 314 (2017) 443–452.
- [48] F. Chen, Q. Yang, X.M. Li, G.M. Zeng, D.B. Wang, C.G. Niu, J.W. Zhao, H.X. An, T. Xie, Y.C. Deng, *Appl. Catal. B* 200 (2017) 330–342.
- [49] B. Wang, L. Guo, T. He, *RSC Adv.* 6 (2016) 30115–30124.
- [50] J. Zhang, Y. Lu, L. Ge, C. Han, Y. Li, Y. Gao, S. Li, H. Xu, *Appl. Catal. B* 204 (2017) 385–393.
- [51] H.J. Li, W.G. Tu, Y. Zhou, Z.G. Zou, *Adv. Sci.* 3 (2016) 1500389.
- [52] F. Ye, H. Li, H. Yu, S. Chen, X. Quan, *Appl. Catal. B* 227 (2018) 258–265.
- [53] N. Tian, H.W. Huang, Y. He, Y.X. Guo, T.R. Zhang, Y.H. Zhang, *Dalton Trans.* 44 (2015) 4297–4307.
- [54] X.Q. Wu, J. Zhao, L.P. Wang, M.M. Han, M.L. Zhang, H.B. Wang, H. Huang, Y. Liu, Z.H. Kang, *Appl. Catal. B* 206 (2017) 501–509.
- [55] A. Iwase, S. Yoshino, T. Takayama, Y.H. Ng, R. Amal, A. Kudo, *J. Am. Chem. Soc.* 138 (2016) 10260–10264.
- [56] H.Y. Li, Y.J. Sun, B. Cai, S.Y. Gan, D.X. Han, L. Niu, T.S. Wu, *Appl. Catal. B* 170–171 (2015) 206–214.
- [57] Z. Pan, T. Hisatomi, Q. Wang, S. Chen, M. Nakabayashi, N. Shibata, C. Pan, T. Takata, M. Katayama, T. Minegishi, A. Kudo, K. Domen, *ACS Catal.* 6 (2016) 7188–7196.
- [58] C.G. Zhou, S.M. Wang, Z.Y. Zhao, Z. Shi, S.C. Yan, Z.G. Zou, *Adv. Fun. Mater.* (2018) 1801214.
- [59] N.K. Veldurthi, N.K. Eswar, S.A. Singh, G. Madras, *Appl. Catal. B* 220 (2018) 512–523.
- [60] Q. Jia, A. Iwase, A. Kudo, *Chem. Sci.* 5 (2014) 1513–1519.
- [61] X.F. Yang, Z.P. Chen, J.S. Xu, H. Tang, K.M. Chen, Y. Jiang, *ACS Appl. Mater. Interfaces* 7 (2015) 15285–15293.
- [62] F. Chen, Q. Yang, Y.L. Wang, J.W. Zhao, D.B. Wang, X.M. Li, Z. Guo, H. Wang, Y.C. Deng, C.G. Niu, G.M. Zeng, *Appl. Catal. B* 205 (2017) 133–147.
- [63] Y. Wang, G.Q. Tan, T. Liu, Y.N. Su, H.J. Ren, X.L. Zhang, A. Xia, L. Lv, Y. Liu, *Appl. Catal. B* 234 (2018) 37–49.
- [64] J. Safaei, H. Ullah, N.A. Mohamed, M.F.M. Noh, M.F. Soh, A.A. Tahir, N.A. Ludin, M.A. Ibrahim, W.N.R.W. Isahak, M.A.M. Teridi, *Appl. Catal. B* 234 (2018) 296–310.
- [65] Z. Wang, J. Lv, J. Zhang, K. Dai, C. Liang, *Appl. Surf. Sci.* 430 (2018) 595–602.
- [66] Z. Liu, X. Xu, J. Fang, X. Zhu, J. Chu, B. Li, *Appl. Surf. Sci.* 258 (2012) 3771–3778.
- [67] M. Xue, J. Ge, H. Zhang, J. Shen, *Appl. Catal. A-Gen.* 330 (2007) 117–126.
- [68] M.S. Zhu, P.L. Chen, M.H. Liu, *J. Mater. Chem.* 22 (2012) 21487–21494.
- [69] X.H. Gao, S.F. Jiang, J. Li, D.H. Ding, S. Gao, G.D. Zheng, *Chin. Sci. Bull.* 39 (1994) 1066–1070.
- [70] M. Yan, Y.L. Wu, Y. Yan, X. Yan, F.F. Zhu, Y.Q. Hua, W.D. Shi, *ACS Sustain. Chem. Eng.* 4 (2016) 757–766.
- [71] B. Dai, X. Tu, W. Zhao, X. Wang, Dennis Y.C. Leung, J. Xu, *Chemosphere* 211 (2018) 10–16.
- [72] S.P. Tandon, J.P. Gupta, *Phys. Status Solidi B* 38 (1970) 363–367.
- [73] Y.K. Zhu, X.L. Zhao, J.Z. Li, H.W. Zhang, S. Chen, W. Han, D.J. Yang, *J. Alloys. Compd.* 764 (2018) 341–346.
- [74] Y.K. Zhu, J. Ren, X.F. Yang, G.J. Chang, Y.Y. Bu, G.D. Wei, W. Han, D.J. Yang, *J. Mater. Chem. A* 5 (2017) 9952–9959.
- [75] X.F. Zhou, C. Hu, X.X. Hu, T.W. Peng, J.H. Qu, *J. Phys. Chem. C* 114 (2010) 2746–2750.
- [76] Y.Q. Yang, G.K. Zhang, S.J. Yu, X. Sheng, *Chem. Eng. J.* 162 (2010) 171–177.
- [77] Y.Y. Li, J.S. Wang, H.C. Yao, L.Y. Dang, Z.J. Li, *J. Mol. Catal. A Chem.* 334 (2011) 116–122.
- [78] L. Shi, L. Liang, J. Ma, F. Wang, J. Sun, *Catal. Sci. Technol.* 4 (2014) 758–765.